Frequency-domain framework for floating installation of wind-turbine towers

Domingos, David Fidalgo; Wellens, Peter; van Wingerden, Jan Willem

DOI
10.1016/j.oceaneng.2024.116952

Publication date
2024

Document Version
Final published version

Published in
Ocean Engineering

Ocean Engineering 297 (2024) 116952

Contents lists available at ScienceDirect

Ocean Engineering

journal homepage: www.elsevier.com/locate/oceaneng

Research paper

Frequency-domain framework for floating installation of wind-turbine towers

David Fidalgo Domingos [a,b,*], Peter Wellens [b], Jan-Willem van Wingerden [a]

[a] Delft Center for Systems and Control, Delft University of Technology, Mekelweg, Delft, 2628 CN, Netherlands
[b] Maritime and Transport Technology, Delft University of Technology, Mekelweg, Delft, 2628 CN, Netherlands

ARTICLE INFO

Keywords:
Heavy lift
Offshore wind
Stochastic disturbances
Workability analysis
Sensitivity analysis
Dynamic error budgeting

ABSTRACT

As a result of more stable wind conditions and the depletion of near-shore locations, wind farms are moving farther offshore into deeper waters, challenging the current limits of offshore heavy-lift operations. This paper presents and verifies a novel frequency-domain framework to perform extensive site-specific analysis, of floating installations of wind-turbine towers, subjected to wind and wave loads. The versatility and potential of this framework is demonstrated with a case-study of a wind farm near the coast of Portugal. The results lead to the following conclusions: (1) Only considering beam-seas the yearly workability is 39 %; (2) Workability is mostly limited by wave loads; (3) Tower motions tend to decrease with tower size and are not significantly affected by hook-tower distance (sling length); and finally, (4) In this case-study the most contributing frequencies for tower motions are 0.3 and 0.4 rad/s, corresponding mainly to the first pendulation mode.

1. Introduction

Current environmental circumstances require an immediate step away from fossil fuels as main energy sources. Therefore, Europe aims at increasing the installed offshore wind power at least 25 times by 2030, compared to the total of 14.6 GW in 2021, Offshore Renewable Energy (2023). As a result of more stable wind conditions and the depletion of near-shore locations, wind farms are moving farther offshore into deeper waters (Ramirez et al., 2019), challenging the current limits of offshore heavy-lift operations.

Initially motivated by the fossil fuel industry in the mid-1950s (Pratt et al., 1997), offshore heavy-lift operations consist of handling large and heavy structures at sea. Given the exposure to weather conditions and the risk involved, safety is of primary importance. Because of the lack of data, the requirement of safety poses challenges when facing new, dynamic and exponentially growing markets, such as offshore wind (Bilgili and Alphan, 2022).

Over time, the design of offshore crane vessels has converged to a semi-submersible crane-vessel (SSCV) type. Although semi-submersibles are known for being sensitive to hanging loads, in comparison to mono-hulls (Nojiri and Sasaki, 1983; Clauss and Riekert, 1990), they provide flexible ballasting and enough deck area to accommodate two cranes of large capacity, outreach and lifting heights (Clauss and Riekert, 1990). In contrast to this, in the offshore wind industry jack-up vessels have been dominating the scene due to higher stability. However, this increased stability comes at a price, which is: operational water depth limit (up to 80 m Next Generation Jack-Up, 2023), dependency on seabed conditions, vulnerability to wind direction changes and jack-up time (Buitendijk, 2016). Limitations that floating vessels can overcome, as shown by Heerema Marine Contractors (HMC), Delft Offshore Turbine (DOT) and Delft University of Technology (TUDelft) with the *FOX* project (TU Delft on Board the World Largest Crane Vessel for Exploring Future Offshore Wind Turbines, 2023). However, ensure that no safety limits are exceeded during the installation of an Offshore Wind Turbine (OWT), it is crucial to have a good understanding of how wind and wave induced motions can be mitigated and how these affect workability, according to the following definition:

> *Workability represents the percentage of time for which a pre-defined operational limit is not exceeded during an installation time-frame.*

The mitigation of load motions is an intrinsic challenge of heavy-lift operations. Some heavy-lift cranes feature heave compensation to control vertical motions by adjusting the cable length (Neupert et al., 2008). However, not every crane has this capability. To address this, Seaqualize has launched a series of semi-active heave compensators that are placed between the hook and the load (Active Heave Compensation, 2023). For horizontal-plane motions, tugger-lines are the to-go choice, despite their limitations in the side-to-side direction. Tugger-winches with constant tension (CT) control (Cozijn et al., 2008) are

* Corresponding author at: Delft Center for Systems and Control, Delft University of Technology, Mekelweg, Delft, 2628 CN, Netherlands.
E-mail address: d.a.fidalgodomingos@tudelft.nl (D.F. Domingos).

https://doi.org/10.1016/j.oceaneng.2024.116952
Received 24 November 2023; Received in revised form 21 January 2024; Accepted 28 January 2024
Available online 16 February 2024

the standard. This method mitigates snap loads, but does not reduce pendulation. In this regard, damping tuggers are a more promising concept (Meskers and van Dijk, 2012; Ku et al., 2013). The field of tugger-line control is an active field of research, an example of this is the holistic approach presented in de Kruif and Rossin (2021), where the interaction of tugger-line control and dynamic-positioning (DP) is studied, showing that actuator usage can be reduced by taking into account this interaction. However, the effect of improving this interaction on yearly workability was outside the scope of the article. In this regard, the approach presented in Clarenburg (2014) addresses this by leveraging the properties of linear frequency-domain methods, reducing the cost of workability calculations by a factor of 1000, which allowed to efficiently explore a larger design space and perform a manual sensitivity analysis of a motion compensated gangway. Given the sheer size of wind farms, every percent of extra downtime is quickly amplified by the large number of operations required, which increases the interest in tailored solutions. This is addressed in specific literature about floating installation of OWTs, most of it can be divided in three categories: installation of foundations (Nejad et al., 2018; Schepers et al., 2022); blade installation (Ren et al., 2018a; Jiang et al., 2018; Ren et al., 2018b, 2019; Gao et al., 2018); and new concepts of vessels and installation methods (Lu et al., 2011; Hoogendoorn et al., 2021; Hong et al., 2023). With a relevant example of research in this field being the work presented in van Beek et al. (2018), where a cost, system dynamics and loads analysis are presented for novel single-lift installation method. This installation method consists of using two cranes simultaneously with a lifting-frame that holds the fully assembled wind turbine by the tower. This research concluded that: (1) The installation of pre-assembled wind-turbines is economically feasible for wind-farms over 1500 MW; (2) Waves can cause guidance pins stabbing outside the buckets; and (3) Using 2-minute wave forecasts can drastically reduce the installation time. However, there are still operational challenges to be overcome, such as: ensuring tower integrity, limitations in crane height capacity, difficult use of heave-compensation, and the need of feeder barges to transport assembled OWT or to facilitate their assembling on-site. From a more scientific perspective, the main limitations of this work lie in the fact that wind loads are neglected and the results are not reproducible, due to intellectual property protection.

Currently, literature lacks information about the workability and dynamics of floating installation of OWT towers, leaving unanswered questions, such as: How should floating installation of wind turbine towers be modelled and how can it benefit from motion compensation? This work aims at making a step towards answering to these questions by developing a mathematical framework that it is used to: Assess yearly workability based on site-specific weather data for head and beam waves; Perform a Sensitivity Analysis, using *Sobol's* global method (Marelli et al., 2022b), to characterize the impact of variations in system parameters on tower motions; And finally, to determine the frequency ranges where the operation is most vulnerable to environmental conditions by means of a Dynamic Error Budgeting analysis (Jabben and van Eijk, 2011; Clarenburg, 2014).

To summarize, the main three contributions of this article are: (1) The development and verification of an open-source frequency-domain framework for floating installation of OWT towers; (2) Assessing the workability of this type of operation based on site-specific weather records; and (3) Providing a better understanding of the effect of wind, waves and system's parameters, on tower motions. Complementary to this, a reference open-source SSCV design is presented, with the intention of stimulating open-research.

This paper is structured in the following way. In Section 2 the structure and derivation of the frequency-domain framework is presented. This is followed by the introduction of a case-study in Section 3, allowing the verification of the framework in Section 4. In Section 5 the results of workability, sensitivity and error budgeting analyses are presented and discussed, in the context of the case-study earlier defined, showing the framework's versatility and potential. This finally leads to the conclusion of this paper, in Section 6.

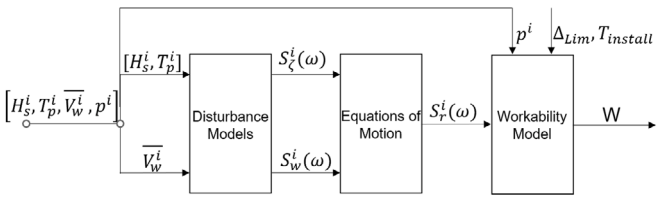

Fig. 1. Framework overview.

2. Mathematical framework

This section presents a frequency-domain framework for floating installation of OWT towers, subjected to stochastic disturbances from wind and waves. The goal is to assess site-specific workability based on weather records and operational limits. Fig. 1 displays the structure of the framework.

As it can be seen, the inputs are: significant wave height (H_s in m); wave peak-period (T_p in s); mean wind speed ($\overline{V_w}$ in m/s); the probability of occurrence (p) of a combination i; the installation tolerance (Δ_{Lim} in m) and the installation time ($T_{install}$ in s). The "Disturbance Models" block is responsible for converting the environmental data into wave and wind power spectral density (PSD), $S_\zeta(\omega)$ and $S_w(\omega)$ in m^2 s and m^2/s, respectively. From here, using the equations of motion of the system, it is possible to determine the response PSD $S_r(\omega)$, in m^2s. Once $S_r(\omega)$ is known, the statistical properties of PSD are used to determine the percentage of time for which the operation can be safely executed, *i.e.:* workability. The following subsections describe in detail each module of the framework.

2.1. Disturbance models

Wind and waves are stochastic in nature, due to turbulence and the superposition of a large amount of wave components, which excites the system in an undesired way, reducing workability. In the context of this work, both wind and waves assumed unidirectional. Wind turbulence is modelled using the *Kaimal* PSD (der Male and Lourens, 2015; Bianchi et al., 2010), given by:

$$S_w(\omega) = \sigma_u^2 \frac{4L_{1u}}{\overline{V_w}(1 + 6\omega L_{1u}/(2\pi\overline{V_w}))^{5/3}} \quad , \tag{1}$$

in which $\overline{V_w}$ represents the mean wind speed in m/s, σ_u is the standard deviation of wind speed ($\approx 0.15 \cdot \overline{V_w}$) and L_{1u} is a turbulence length scale in meters ($\approx$175 m) (Bianchi et al., 2010). Note that in the context of this framework, $\overline{V_w}$ represents the mean wind speed at the tower centre of gravity.

Irregular waves are modelled using the JONSWAP PSD (Journée et al., 2015), which is described by the following expression:

$$S_\zeta(\omega) = \frac{320 {H_s}^2 \cdot \omega^{-5}}{{T_p}^4} \cdot e^{\frac{-1950\omega^{-4}}{T_p^4} \cdot \gamma^A} \quad , \tag{2}$$

where γ is the peakness factor (often assumed to be 3.3), A is an exponential function of the peak-period T_p, and σ a step function which assumes different values for the range of frequencies below and above the peak frequency. More details can be found in Journée et al. (2015).

The first block in the framework consists of these two spectra. In the coming section, a mathematical model is derived which allows correlation of output disturbances PSD with tower motions.

2.2. Equations of motion

Reduced-order models describe systems working within a narrow operational range such that the governing physical laws can be approximated to their local solutions. Their simplicity and reduced computational cost allow to explore wider design spaces and provide a more

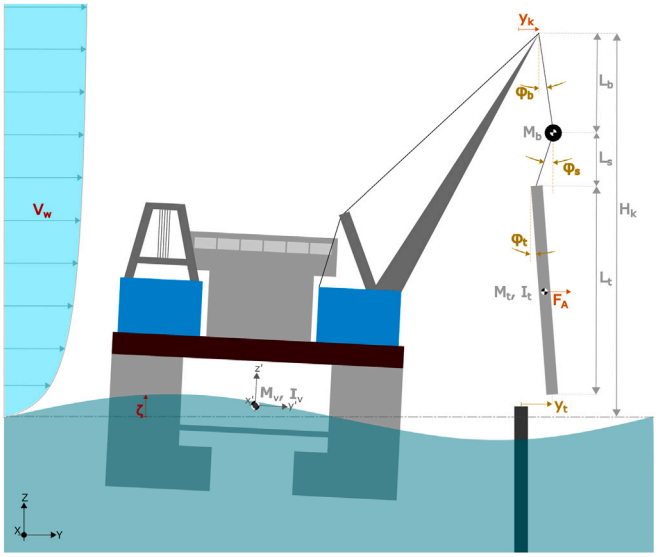

Fig. 2. Diagram describing system parametrization.

clear perspective on the role of specific physical phenomena on the system behaviour. An example of this, is the work presented in Bos and Wellens (2021), where a reduced order model is used to provide a better understanding of the fluid–structure interaction between regular waves and a simple pendulum.

To derive a reduced-order model it is necessary to define frames of reference and parameterize the system. Two frames or reference are adopted in this research, an inertial one ([X,Y,Z], earth-fixed) and an non-inertial one ([x',y',z'], ship-fixed), as shown in Fig. 2, below. The non-inertial frame of reference is located at the vessel's centre of gravity with the x-axis pointing towards the bow, the y-axis pointing towards port-side and the z-axis perpendicular to the undisturbed water surface, according to the right hand convention. The parameters shown in Fig. 2 characterize the system. The sources of disturbances (in red) are: wind speed (V_w) and wave elevation (ζ). The disturbances (in orange) are: crane tip motion (y_k) and aerodynamic force (F_A). The variables that describe the states of the system (in yellow) are: off-lead angle (ϕ_b), sling angle (ϕ_s), tower angle (ϕ_t) and the distance between the tower bottom and foundation (y_t). And finally, (in grey), the properties of the system: mass and inertia of the vessel (M_v, I_v), hook block mass (M_b), tower mass and inertia (M_t, I_t), length of the hook block cable (L_b), sling (L_s) and tower (L_t), and finally, crane tip height (H_k). For simplicity, the system is modelled in 2D by assuming long-crested waves. Given this, the next step is to model the effect of disturbances on the system by deriving the governing equations.

2.2.1. Wave induced motions

The wave loads are composed of a mean-component, low-frequency component and a high frequency component (Journée et al., 2015). In the context of this research, only the high-frequency component (first-order wave loads) are considered. The interaction of current and second-order low-frequency wave loads with the vessel's dynamic positioning (DP) system can induce slow varying motions on the vessel. Given their low frequency, these are not expected to significantly excite tower pendulation. Therefore, in this paper it is assumed that the DP system perfectly cancels these motions. It has been shown in the literature that there is a degree of interaction between the DP and pendulation control system (de Kruif and Rossin, 2021), in future work it would be interesting to assess impact the DP performance on workability.

The wave induced motions are considered to be linear and frequency dependent (Journée et al., 2015). They are described using response amplitude operators (RAOs). These can be obtained using potential-flow panel-methods (Journée et al., 2015), and map wave-amplitudes to steady-state ship motions, as follows:

$$RAO_r(\omega) = \frac{r_a(\omega)}{\zeta_a(\omega)} \Rightarrow \begin{cases} |RAO_r(\omega)| = \sqrt{RAO_r(\omega) \cdot RAO_r(\omega)^*} \\ \angle RAO_r(\omega) = arctan\left(\frac{Im\{RAO_r(\omega)\}}{Re\{RAO_r(\omega)\}}\right) \end{cases},$$
$$[r_a(\omega), \zeta_a(\omega)] \in \mathbb{C}, \tag{3}$$

where $r_a(\omega)$ and $\zeta_a(\omega)$ are complex numbers representing the system response and wave amplitudes in meters, respectively. The norm of $RAO_r(\omega)$ represents the amplitude of the relative response and the argument the phase angle, in radians. Note that $*$ represents the complex conjugate. Since turbine towers are likely to represent less than 1% of a SSCV's displacement, tower to vessel interactions are considered negligible, and therefore the use of RAOs in this context deemed valid (Nojiri and Sasaki, 1983; Clauss and Riekert, 1990). Given this, the vessel's response PSD is as follows (Journée et al., 2015):

$$S_{r,k}(\omega) = S_\zeta(\omega) \cdot |RAO_r(\omega)|^2 \quad , \tag{4}$$

in which $S_\zeta(\omega)$ is the wave energy spectra, as previously introduced.

2.2.2. Wind loads

In contrast to traditional heavy-lift installations, wind disturbances are believed to be important in the context of OWT installations, given the light weight of the components and the fact that these installations take place in regions of high wind energy. In order to simplify the problem, it is assumed that the wind turbine tower is a perfect cylinder; the aerodynamic centre of pressure is located at the tower's centre of gravity (CoG); wind disturbance is caused by aerodynamic drag. Furthermore, it is also considered that vessel's wind-induced motions are much smaller and of much lower frequency than wave-induced motions. Therefore, not being expected to significantly contribute to OWT tower motions. A quantitative assessment of these motions is recommended for future work. Given this, the aerodynamic force, F_A in Fig. 2, acting on the tower is described as follows (Bishop and Hassan, 1964):

$$F_A = \frac{1}{2}\rho_{air} V_w'^2 D_t L_t C_D \quad , \tag{5}$$

in which, ρ_{air} represents the air density in kg/m^3, V_w' the relative wind speed in m/s, C_D the drag coefficient of a cylinder, and D_t and L_t the tower diameter and length in m. The expression for the relative wind speed is:

$$V_w' = V_w - \dot{y}_{t,CoG} \quad , \tag{6}$$

where $\dot{y}_{t,CoG}$ is the velocity of the tower's CoG, in m/s. By substituting the previous equation into the aerodynamic force expression, Eqs. (5) and (6), the latter can be decomposed into an aerodynamic excitation component (F_A^{exc}) and damping component (F_A^{damp}), as follows:

$$F_A = \frac{1}{2}\rho_{air}(V_w - \dot{y}_{t,CoG})^2 D_t L_t C_D \Rightarrow$$
$$\Rightarrow \begin{cases} F_A^{exc} = \frac{1}{2}\rho_{air} D_t L_t C_D V_w^2 \approx \frac{1}{2}\rho_{air} D_t L_t C_D \overline{V_w} V_w = E_A V_w \\ F_A^{damp} = \frac{1}{2}\rho_{air} D_t L_t C_D (-2V_w \dot{y}_{t,CoG} + \dot{y}_{t,CoG}^2) \\ \approx -\rho_{air} D_t L_t C_D \overline{V_w} \dot{y}_{t,CoG} = -b_A \dot{y}_{t,CoG}, \end{cases} \tag{7}$$

where E_A and b_A are the aerodynamic excitation and damping coefficients, in Ns/m, both functions of mean-wind speed ($\overline{V_w}$). The expressions are linearized in order to allow a linear frequency-domain representation. Given that $\dot{y}_{t,CoG}$ is much smaller than typical wind speeds, $\dot{y}_{t,CoG}^2$ is neglected. The linear expression for the aerodynamic damping force only ensures damping for non-zero wind-speeds, which is a realistic setting. In the coming section this is addressed by introducing an extra damping term b_{sys}.

2.2.3. System dynamic model

While previous sections modelled the environmental disturbances acting on the system, y_k and F_A, this section models the system response using the *Lagrange* method, presented as follows:

$$\frac{\partial}{\partial t}\left(\frac{\partial T(q_i)}{\partial \dot{q}_i}\right) - \frac{\partial T(q_i)}{\partial q_i} + \frac{\partial R(q_i)}{\partial \dot{q}_i} + \frac{\partial U(q_i)}{\partial q_i} = Q_i \quad , \tag{8}$$

in which q_i represents an independent coordinate system of each degree of freedom, in this case: block angle ϕ_b, sling angle ϕ_s and tower angle ϕ_t, all in rad. $T(q_i)$, $U(q_i)$ and $R(q_i)$ are functions of q_i, representing the system's kinetic, potential and dissipative energies, in J. Q_i represents the external loading applied to each q_i. In order to determine these expressions, the system is simplified to a 2D, driven, tripe-pendulum with a distributed mass. Given this, the crane tip position, relative to the initial condition is:

$$\vec{p}_k = (y_k - y_k^0)\,\vec{j} + (z_k - z_k^0)\,\vec{k} \quad , \tag{9}$$

in which y_k and z_k are the horizontal and vertical coordinates of the crane tip, in m. The superscript 0 represents undisturbed initial conditions. $\vec{j}$ and $\vec{k}$ are unit vectors in the Y and Z axis, respectively. From this, the block and tower position vectors, $\vec{p}_b$ and $\vec{p}_{t,CoG}$, are given by:

$$\begin{cases} \vec{p}_b = \vec{p}_k + L_b\left(sin\phi_b\,\vec{j} + (1 - cos\phi_b)\,\vec{k}\right) \\ \vec{p}_{t,CoG} = \vec{p}_b + L_s\left(sin\phi_s\,\vec{j} + (1 - cos\phi_s)\,\vec{k}\right) \\ \quad + \frac{L_t}{2}\left(sin\phi_t\,\vec{j} + (1 - cos\phi_t)\,\vec{k}\right) \end{cases} \tag{10}$$

From here, analytical expressions can be derived for the potential $U(\phi_b, \phi_s, \phi_t)$, kinetic $T(\phi_b, \phi_s, \phi_t)$ and dissipative $R(\phi_b, \phi_s, \phi_t)$ energies of the system, as well as for the external loading Q_i:

$$\begin{cases} U(\phi_b, \phi_s, \phi_t) = g(M_b z_b + M_t z_t) \\ T(\phi_b, \phi_s, \phi_t) = \frac{1}{2}\left(M_b|\dot{\vec{p}}_b|^2 + M_t|\dot{\vec{p}}_{t,CoG}|^2 + I_t\dot{\phi}_t^{\,2}\right) \\ R(\phi_b, \phi_s, \phi_t) = \frac{1}{2}\left(b_A\dot{y}_{t,CoG}^2 + b_{sys}\dot{y}_b^2\right) \\ Q_b = L_b E_A V_w \\ Q_s = L_s E_A V_w \\ Q_t = \frac{L_t}{2} E_A V_w, \end{cases} \tag{11}$$

where the subscripts b, s and t refer to the coordinates ϕ_b, ϕ_s and ϕ_t, see Fig. 2. b_{sys} is an additional generic damping coefficient term, in Ns/m, which accounts for mechanical losses of the system (*e.g.*: sheaves and cables) aerodynamic damping at non-zero wind-speeds and energy dissipated by the vessel through water viscosity. Note that the dot on top of a vector is used to represent a time derivative, analogous to $\frac{\partial}{\partial t}$.

By combining the Eqs. (8) and (11), the dynamic model of the system is obtained. To ensure linearity, small angle approximation is adopted and the vertical motion of the crane tip neglected, as follows:

$$\begin{cases} z_k = \dot{z}_k = \ddot{z}_k \approx 0 \\ sin(\phi) \approx \phi \\ cos(\phi) \approx 1, \end{cases} \tag{12}$$

in which ϕ is representative of ϕ_b, ϕ_s and ϕ_t. Although neglecting crane tip vertical motion can affect the pendulation behaviour, it is not expected to significantly affect workability since side-to-side accelerations are expected to be much larger.

A common way to represent coupled ordinary differential equations is with state-space modelling. A variety of tools is implemented in common programming languages to manipulate, analyse and solve this type of system, making it convenient to use. In the coming section the equations of motion, here derived, are represented in this form.

2.2.4. State-space model

The general form of a state-space representation is:

$$\begin{cases} \dot{x} = Ax + Bu \\ y = Cx + Du, \end{cases} \tag{13}$$

where A is the dynamics matrix, B the input matrix, C output matrix and D the direct term matrix. x, u and y are the state, input and output vectors, which in the context of this problem are:

$$x = \begin{bmatrix} \dot{y}_k \\ y_k \\ \dot{\phi}_b \\ \phi_b \\ \dot{\phi}_s \\ \phi_s \\ \dot{\phi}_t \\ \phi_t \end{bmatrix}, u = \begin{bmatrix} \ddot{y}_k \\ V_{wind} \end{bmatrix}, y = \left[y_k + L_b\phi_b + L_s\phi_s + L_t\phi_t\right], \tag{14}$$

in which the inputs of the system are crane tip acceleration ($\ddot{y}_k$) and wind speed (V_w). The output is the tower bottom position, y_t. Since the latter requires a double integration of the crane tip acceleration signal, a second-order high-pass filter is added to mitigate numerical drift:

$$\begin{bmatrix} \ddot{y}_k \\ \dot{y}_k \end{bmatrix} = \begin{bmatrix} -2\zeta_f\omega_c & -\omega_c^2 \\ 1 & 0 \end{bmatrix}\begin{bmatrix} \dot{y}_k \\ y_k \end{bmatrix} + \begin{bmatrix} 1 \\ 0 \end{bmatrix}\left[\ddot{y}_k\right], \tag{15}$$

where ζ_f it is the damping ratio of the filter and ω_c the cut-off frequency, in rad/s.

Conventionally, the A, B, C and D matrices have constant values. However, both the aerodynamic excitation $E_A(\overline{V_w})$ and damping $b_A(\overline{V_w})$ coefficients are functions of the mean wind speed $\overline{V_w}$, as shown in Eq. (7), meaning that matrix A and B are functions of $\overline{V_w}$.

2.2.5. Frequency response

The state-space model can be converted to the frequency-domain using the *Laplace* transform (Johan Åström and Murray, 2021). With s being the complex frequency-domain parameter, the system can be described by the following two transfer functions:

$$\begin{cases} G_{\zeta,r}(s) = \frac{R(s)}{Z(s)} \\ G_{w,r}(s) = \frac{R(s)}{V_w(s)}, \end{cases} \tag{16}$$

in which $R(s)$ represents the system response (tower bottom motion), $Z(s)$ the wave elevation and $V_w(s)$ the wind speed, all in the *Laplace* space. Analogously to Eq. (4), the responses PSD of the system, $S_{\zeta,r}(\omega)$ and $S_{w,r}(\omega)$, are given by:

$$\begin{cases} S_{\zeta,r}(\omega) = S_\zeta(\omega)\cdot|G_{\zeta,r}(i\omega)|^2 \\ S_{w,r}(\omega) = S_w(\omega)\cdot|G_{w,r}(i\omega)|^2, \end{cases} \tag{17}$$

where the normal $|G_{\zeta,r}(i\omega)|$ and $|G_{w,r}(i\omega)|$ are gain spectra of the respective transfer functions (Johan Åström and Murray, 2021). Given the stochastic nature of wave and wind induced motions, the phase angle ϵ of the spectrum is described by a uniform probabilistic distribution in the range of $[0, 2\pi]$ rad/s, Journée et al. (2015). Thus, the response PSD $S_r(\omega)$ of the system, subjected to wind and waves, is given by:

$$S_r(\omega) = S_{\zeta,r}(\omega)e^{i\epsilon_\zeta} + S_{w,r}(\omega)e^{i\epsilon_w} \tag{18}$$

This step completes the equations of motion block in Fig. 1. In the coming section, the last block of the framework is described, concerning the workability model.

2.3. Workability model

For the successful installation of a wind-turbine tower, it is necessary to ensure that no operational safety limits are exceeded. The goal of the workability model derived in this section is to rapidly assess whether or not an installation can be completed, based on site-specific environmental conditions. For this the following definition of workability is adopted:

Workability (W) represents the percentage of time for which a pre-defined operational limit (Δ_{lim}) is not exceeded during the installation time-frame ($T_{install}$).

This can be assessed by making use of the statistical properties of the response PSD of the system, $S_r(\omega)$. According to Journée et al. (2015), the amount of times (N_{exc}) that an operation limit (Δ_{lim}) is expected to be exceeded during the installation time ($T_{install}$) is given by:

$$N_{exc} = \frac{T_{install}}{T_{2r}} \cdot P\{r > \Delta_{lim}\} \quad , \tag{19}$$

where T_{2r} denotes the average zero-crossing period of the system response, and $P\{r > \Delta_{lim}\}$ the probability of the response exceeding the operational limit Δ_{lim}, with the former being given by:

$$T_{2r} = 2\pi \cdot \sqrt{\frac{m_{0r}}{m_{2r}}} \quad , \tag{20}$$

in which m_{nr} denotes the nth order moment of $S_r(\omega)$:

$$m_{nr} = \int_0^\infty \omega^n \cdot S_r(\omega) d\omega \quad , \tag{21}$$

According to Journée et al. (2015), $S_r(\omega)$ can be assumed narrow banded. In this case the cumulative probability function of the system response is approximated by a *Rayleigh* distribution:

$$P\{r > \Delta_{lim}\} = e^{\frac{-\Delta_{lim}^2}{2m_{0r}}} \quad . \tag{22}$$

From the workability definition we find that a condition is workable if the expected number of times that an operational limit is exceeded is lower than 1, *i.e.:* $N_{exc} < 1$. This results in a binary condition: workable or not workable. Using the probability of occurrence p^i of an environmental condition i, it is then possible to compute workability W, as follows:

$$W = \sum_{i=1}^{N} p^i \cdot \delta(N_{exc}^i) \quad , \tag{23}$$

in which N represents all the existing combinations of sea-states, p^i the respective probability of occurrence and $\delta(N_{exc}^i)$ a Dirac function:

$$\delta(N_{exc}^i) = \begin{cases} 1 & , N_{exc}^i < 1 \\ 0 & , N_{exc}^i \geq 1 \end{cases} \tag{24}$$

3. Case-study

Research about floating installation of OWTs has been increasing in recent years, as jack-up vessels start not to suffice the demands of the market. However, intellectual property regulations of offshore companies are strict, which often limits open-research in this field. To overcome this, in this section a case-study is presented, in which an open-source semi-submersible crane-vessel (SSCV) is performing the installation of DTU 10 MW wind turbine towers near the Portuguese coast. This case focuses on the final tower installation stage, in which the bottom end of the tower is suspended 3 m above the foundation waiting for a weather window for the set-down. Below, Fig. 3 shows the open-source crane-vessel, which we name SSCV Prometheus.

Prometheus is a 160 m semi-submersible crane-vessel, representative of existing ones of its kind. For the sake of results reproduction, its design consists of straight lines. Table 1 describes the main characteristics.

The 3D geometry, as well as response amplitude operators and hydrostatic data are publicly available (Domingos et al., 2023). The vessel and crane are considered as one rigid body. In this case-study two operational conditions are considered: (1) Head wave, installing the tower over the bow, the vessel is free to surge and pitch; (2) In beam waves installing the tower over star-board, in which it sways and rolls.

The wind-turbine tower is inspired by the *DTU 10 MW* reference wind turbine, Bak et al. (2013). It is 115 m tall, with a diameter of

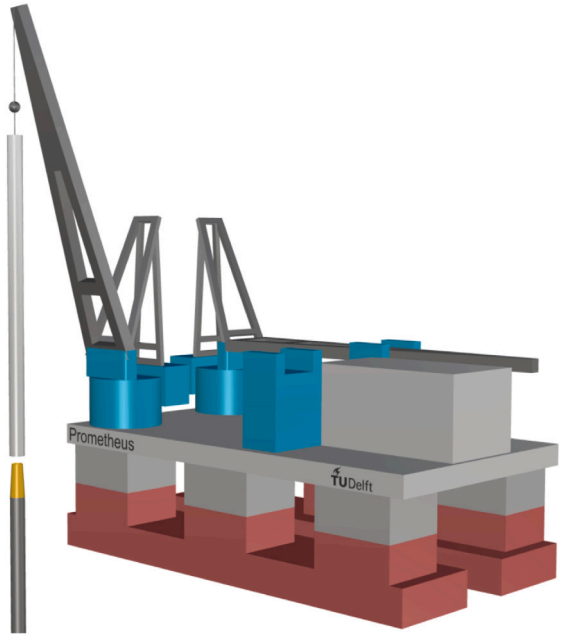

Fig. 3. Prometheus, an open-source SSCV (Domingos et al., 2023).

Table 1
Prometheus' characteristics (Domingos et al., 2023).

Description	Notation	Value	Unit
Length Overall	LOA	160	m
Beam	B	90	m
Draft	D	25	m
Submerged Volume	∇	196 250	m^3
Transverse Metacentric Radius	BM_t	25.4	m
Longitudinal Metacentric Radius	BM_l	56.8	m

5.5 m and a weight of 600 ton. The location of the installation is inspired by a recent tender for 10 GW of offshore wind energy to be installed before 2030 in Portugal (Portugal to Launch First Offshore Wind Auction, Eyes 10 GW by 2030, 2023). One of the designated areas, Figueira da Foz wind park, Fig. 4, is planned to have an installed capacity of 4 GW. Located at an average water-depth of over 100 m, as shown in Fig. 4 below, this wind park is beyond the depth-limits of any currently existing jack-up vessel (Next Generation Jack-Up, 2023). The great exposure to Atlantic swell, makes the Figueira da Foz wind park a relevant case-study for floating installation of OWTs.

The operational limits here considered are: installation tolerance (*i.e.:* the allowable misalignment between the tower and the foundation) and the maximum off-lead angle (ϕ_b), a mechanical limitation of the crane. Regarding the installation time-frame ($T_{install}$), van Beek et al. (2018) considers 65 s. This accounts for set-down time, thinking time and mechanical system delays. However, this value does not include monitoring time and buffer time in case any of any extra delay. Thus, 120 s is considered to be a more realistic time interval to ensure a safe operation.

Site-specific weather data is obtained from satellite measurements, publicly available in ESOX (2023). These records consist of 30 years of hourly measurements of sea-states and average wind speeds, between the years of 1990 and 2019. The wind-speeds are interpolated to the vertical position of the tower's CoG using a boundary-layer power-law (Kundo et al., 2016).

All the relevant parameters describing this case-study are to be found in Table 2. The coming section uses this case study to validate the framework previously presented, against a high-fidelity model.

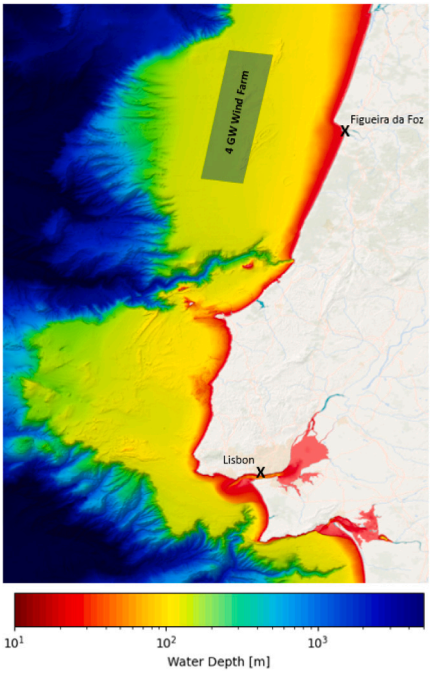

Fig. 4. Location of Figueira da Foz wind farm (Ministerios: Economia e Mar, Ambiente e Acao Climatica e, Infraestruturas e Habitacao, 2023) and bathymetric map (Map Viewer, 2023).

Table 2
Case-study parameters.

Description	Notation	Value	Unit
Crane tip height	H_k	176	m
Block cable length	L_b	35	m
Sling length	L_s	10	m
Tower height	L_t	115	m
Tower diameter	D_t	5.5	m
Hook block mass	M_b	50×10^3	kg
Tower mass	M_t	600×10^3	kg
Tower moment of Inertia	I_t	66.125×10^7	kgm^2
Installation tolerance	$\Delta^{y_t}_{lim}$	1.5	m
Off-lead angle limit	$\Delta^{\phi_b}_{lim}$	3	deg
Installation time-frame	$T_{install}$	120	s
Sea-water density	ρ_w	1025	kg/m^3
Air density	ρ_{air}	1.293	kg/m^3
Tower drag coefficient	C_D	0.65	–
Additional system damping	b_{sys}	17	kNs/m
Installation site coordinates	N-E	40.25–9.5	deg

4. Verification of wave induced motions

Model verification is an essential step in the development process of a mathematical model. Inspired by Makarov and Harada (2022), this section makes a direct comparison between a *WEC-Sim* model and the mathematical model previously presented in this paper. The case-study introduced in the previous section is used for the verification of wave induced motions. In future research it is recommended to verify wind induced motions recurring to CFD, for more accurate aerodynamic force estimations.

4.1. Hydrodynamic calculations

WEC-Sim is a open-source, multibody, non-linear, time-domain solver for floating bodies (Ogden et al., 2022; Makarov and Harada, 2022). The hydrodynamic data required by *WEC-Sim* to determine wave loads is computed, in this paper, using the diffraction code *Capytaine* (Ancellin and Dias, 2019; Babarit and Delhommeau, 2015). From this hydrodynamic data, crane tip acceleration RAOs are also computed, which are used by the framework, under the assumption of negligible tower to vessel interaction

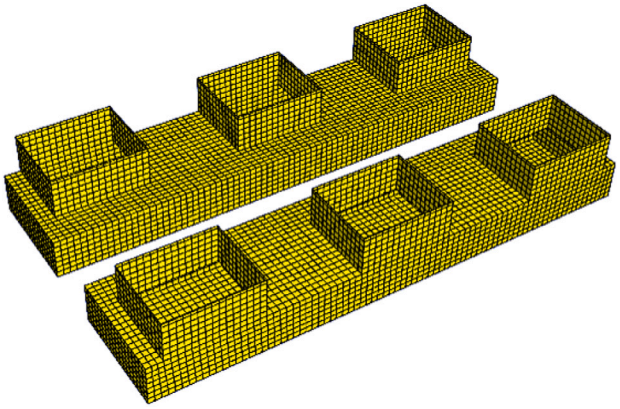

Fig. 5. Prometheus SSCV mesh for BEM calculations.

Fig. 5 shows the mesh for the diffraction calculations. It is composed of 2D quadrangles, with a reference size of 2 m, fulfilling *Capytaine's* recommendations: maximum element size needs to be smaller than $\lambda(\omega_{max})/8$, where $\lambda(\omega_{max})$ represents the shortest wave length of interest. This mesh was obtained using the open-source meshing software *Salome* (Salome Mesh User's guide: Introduction to Mesh, 2023). For the *Capytaine* calculations, the wave frequency range varies according to the range $\omega = [10^{-2}; 2]$ rad/s in steps of 10^{-2} rad/s.

In the present case, the distance from the top of the floaters to the free-surface is of 12.5 m. Numerical instabilities of the BEM code were observed for shallower drafts, when this distance becomes 10 m or less. It is caused by the presence of panels with normals pointing towards the free-surface (Kroft et al., 2022). The hydrodynamic characteristics of Prometheus can be also found in Domingos et al. (2023), as well as geometry and other relevant information such as mass, draft, moments of inertia, among others. The crane tip acceleration is as follows:

$$RAO_{\ddot{y}_k}\vec{j} = -\omega^2\left(RAO_{sway}\vec{j} + H_k\vec{k} \times RAO_{roll}\vec{i}\right) \quad , \tag{25}$$

in which H_k is the crane tip height (Table 2), RAO_{sway} the response amplitude operator in sway and RAO_{roll} in roll. Note that $[\vec{i}, \vec{j}, \vec{k}]$ are unit vectors representing the axis $[X, Y, Z]$ of the earth fixed frame of reference, respectively.

4.2. Verification results

The *WEC-Sim* simulator setup is shown in Fig. 6.

A beam-sea characterized by a *JONSWAP* spectrum with 8 s peak-period (T_p) and 3 m significant wave height (H_s) is chosen as a representative limiting condition. Given the stochastic nature of the disturbances and the relevance of the statistical properties of the system's response spectra in the context of this work, cumulative standard deviation, $c\sigma(\omega_n)$, is chosen as a verification criterion:

$$c\sigma(\omega_n) = \sqrt{m_0(\omega_n)} = \sqrt{\int_0^{\omega_n} S_r(\omega)d\omega}, \tag{26}$$

where ω_n represents a discrete frequency n, in rad/s. This criterion provides detailed information about the contribution of each frequency to the total standard deviation. To obtain the tower-bottom motion PSD from WEC-Sim, the time trace is first converted into an amplitude spectrum $y_t(\omega_n)$ using Fast Fourier Transform (FFT) and then normalized by the discretization frequency $\Delta\omega$ in the following manner (Journée et al., 2015):

$$S_r(\omega_n) = \frac{y_t^2(\omega_n)}{2\Delta\omega}, \tag{27}$$

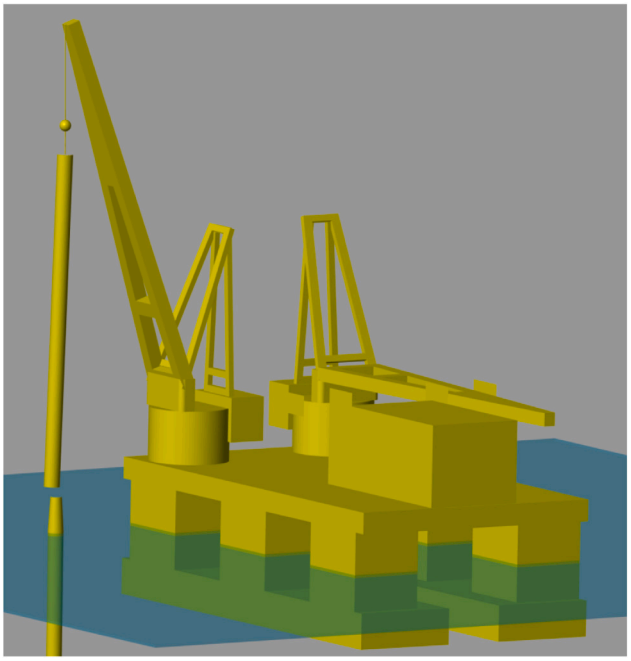

Fig. 6. *WEC-Sim* setup for the verification.

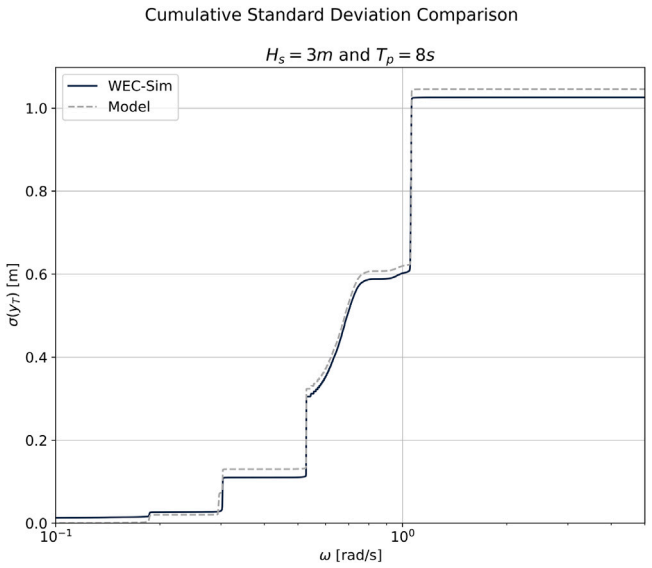

Fig. 7. Comparison of cumulative standard deviation of tower bottom motions between the framework's model and a WEC-Sim model.

Fig. 7 shows good agreement between the WEC-Sim model and the framework model in terms if the cumulative standard deviation. While the framework's mathematical model over-estimates the response amplitude by 2%, it perfectly predicts the main contributing frequencies to the standard deviation. The 2% difference between the framework model and *WEC-Sim* is thought to originate from tower to vessel interaction. The difference is small enough to consider the framework verified.

5. Results and discussion

This section aims at providing a better understanding of the floating installation of OWT towers, by answering to a number of questions that literature has not answered yet, such as: What is the expected yearly workability? Is head-seas the most favourable condition? What are the most important system parameters? Are waves the main source of disturbance?

This type of insight is important for the improvement of floating offshore operations. Therefore, this section applies the framework presented in this paper to the case-study defined in Section 3. It answers the previous questions, while demonstrating the versatility and potential of the framework.

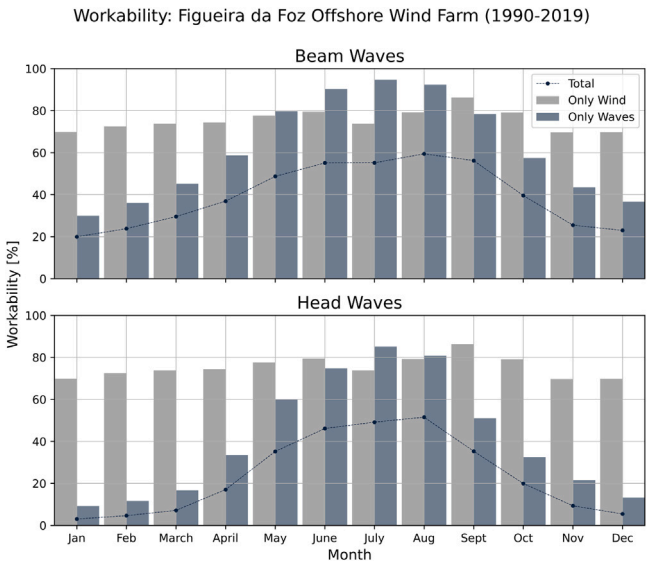

Fig. 8. Workability at Figueira da Foz offshore wind farm in beam and head seas.

5.1. Workability

In Fig. 8, the workability of this operation is assessed and compared for beam and head waves, on the monthly basis.

The grey bars represent the workability if only assessed considering wind, therefore, independent from wave direction. The blue bar represents workability when only considering wave induced motions. Finally, the dark blue dots connected by a dashed line, represent the total workability, *i.e.* the workability considering wind and waves. As can be expected, the summer period is the one with higher workability (50%–60%), in contrast to winter. It is also possible to see that workability is mainly limited by wave induced motions, except in some summer months, explaining the popularity of jack-up vessels. Also, the total workability is significantly lower than any of the previous two, stressing the importance of considering waves as well as wind in planning of operations. Perhaps, a less intuitive observation, is the fact that the most limiting wave direction is head-seas, with an average yearly workability of 24% compared to the 39% in beam-seas. This difference is caused by the higher hydrostatic stiffness in pitch than in roll, leading to larger crane-tip accelerations. During the simulations it was also possible to observe that a 3 degrees off-lead angle limit is seldomly reached. A projection based on these results and field data (Installation Time, 2023) suggests that it would take from 4 to 5 years for this vessel to perform the installation of *Figueira da Foz* wind farm.

5.2. Sensitivity analysis

A sensitivity analysis is a type of analysis that characterizes the impact of variations in system parameters on the output. This information provides a better understanding of a system's behaviour, which is useful from the operational point of view, as well as from the modelling point of view. It allows for quantification of model uncertainties, and identifies unnecessary parameters in an informed

Table 3
Parameter's variation intervals for sensitivity analysis.

Description	Notation	Interval	Unit
Sling length	L_s	[2.5; 17.5]	m
Tower height	L_t	[90; 140]	m
Hook block mass	M_b	[25; 75] × 10^3	kg

way. Most of the approaches for sensitivity analysis can be split in three groups: Sample-based methods, Linearization methods and Global methods (Marelli et al., 2022b). In the context of this research a global method is adopted via *Sobol's Sensitivity*. This method performs an evaluation of the model at different working points by means of a Monte-Carlo simulation. Then the variance of the model output is related to the variance of each parameter (Meloni and Dellino, 2015), being the reason why this method is also known as *ANOVA* (ANalisys Of VAriance). There are first-order *Sobol's* indices and higher-order ones. While the first-order ones assess the impact of varying individual parameters, higher-order indices assess the impact of varying combinations of parameters. Despite the fact that the computational cost increases linearly with the order of the indices (Marelli et al., 2022b), in the context of this research, the added value of considering higher-order *Sobol* indices is not considered significant, and therefore neglected. The sensitivity analysis is performed with the open-source software *UQLab* (Marelli et al., 2022a).

The system sensitivity to parameter variations is assessed based on the tower bottom's motion standard deviation (σ). The environmental conditions are: 8 s peak-period (T_p), 3 m significant wave height (H_s) and 10 m per second average wind speed ($\overline{V_w}$). In order to ensure physically meaningful sets of parameters, the system is reduced to 3 independent variables: sling length (L_s), tower length (L_t) and hook block mass (M_b). Table 3 contains the intervals for which each parameter was varied, using a uniform probabilistic distribution.

According to dimensional analysis, the remaining variables are functions of tower length (L_t):

$$\begin{cases} L_b = h_{k0} - L_s - L_t - \Delta z_0 \\ D_t = D_{t0}\left(\frac{L_t}{L_{t0}}\right) \sim L_t \\ M_t = M_{t0}\left(\frac{L_t}{L_{t0}}\right)^3 \sim L_t^3 \\ I_t = \frac{1}{12} M_t L_t^2 \sim L_t^5, \end{cases} \tag{28}$$

where Δz is the 3 m clearance between the tower bottom and the foundation, and the subscript 0 refers to the reference values defined in Table 2. The crane tip height (H_k) is kept constant to ensure the same operational setting between simulations. The *Sobol's* sensitivity indices shown in Fig. 9, below, are computed from a sample of 1250 Monte Carlo simulations. According to these results, tower length (L_t) is the parameter that affects tower bottom motions the most, by a large margin, independently from wave direction. Hook block mass (M_b) is the second most relevant parameter, especially in beam waves, since it affects the stiffness of the second pendulation mode. However, not as much as tower size, since $M_t \sim L_t^3$. The least important parameter is sling length (L_s), showing a very limited influence on the results. This is explained by the fact that the sling length is only relevant for the third pendulation mode, which occurs at frequencies above 2 rad/s, near which the wave spectrum has minimal energy content. This result is particularly interesting, since it indicates that the degree of freedom ϕ_b might be superfluous. It is expected that neglecting it can reduce the computational cost of the model and its derivation by over 50 % (assuming Gaussian elimination), while having a limited impact on the relevance of the results.

Although *Sobol* sensitivity provides useful information about how much variations in the system's parameters can affect the output, it does not provide information about in which way the response is affected. In order to assess this, the 3D surface plot of Fig. 10 shows,

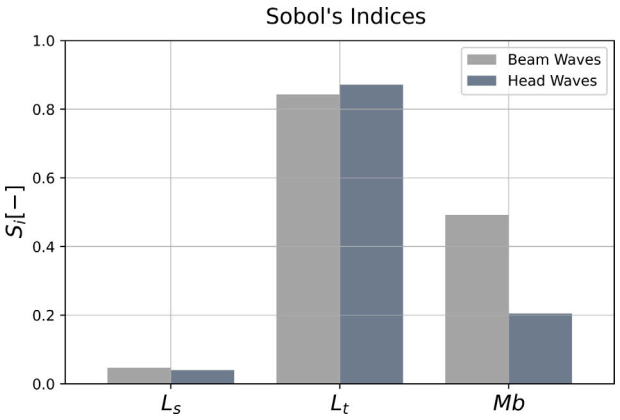

Fig. 9. *Sobol's* sensitivity indices.

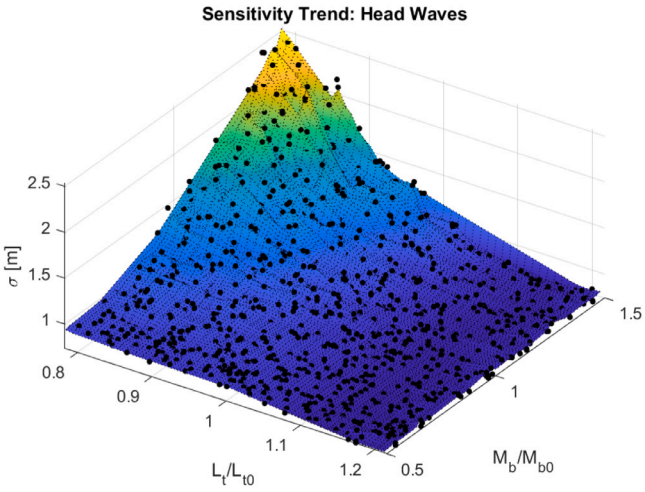

Fig. 10. Surface plot showing the effects of varying tower length (L_t) and hook block mass (M_b) on the standard deviation (σ) of the tower bottom position.

for the case of beam waves, the explored design space, neglecting the variation sling length. The black dots are the data points from the *Monte Carlo*. The 3D surface is the result of a linear interpolation between *Monte Carlo* data points. Looking at this data, it is possible to identify clear trends. Tower bottom motions increase with block weight (M_b) and decrease with tower length (L_t). Following the same reasoning as before, increasing block mass decreases the natural frequency of the second pendulation mode, bringing it closer to wave excitation frequencies. While increasing tower size increases the natural frequency of the second pendulation mode (away from wave excitation) as well as making the system more resilient to wind gusts. The scaling law for tower weight (Eq. (28)) also explains why for larger towers the effect of varying block mass is of less importance than for smaller towers. It is not intuitive that when these results are extrapolated to workability, that workability increases with tower size. To confirm this hypothesis a similar study must be conducted assessing workability. However, it is important to ensure that tower to vessel interactions remain irrelevant for larger tower sizes, according to the current assumptions of the framework.

5.3. Disturbance analysis

Although the analysis provide a picture of the system limitations and behaviour, they do not provide information about what frequencies are limiting workability the most. In this section, this is assessed using *Dynamic Error Budgeting* (DEB) (Jabben and van Eijk, 2011; Clarenburg,

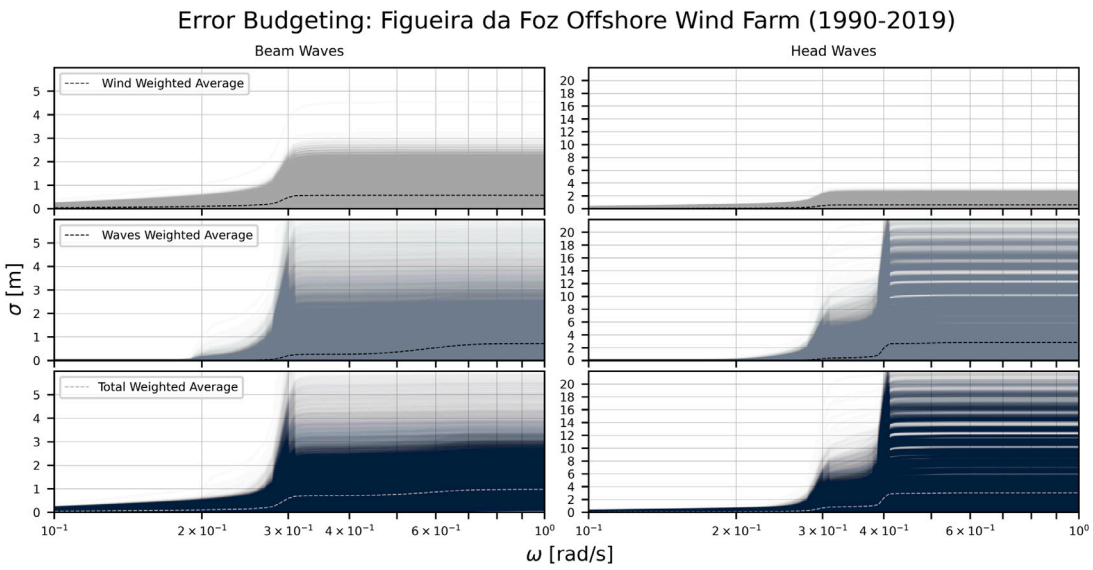

Fig. 11. Error budgeting for all the recorded combinations of weather conditions from 1990 to 2019, for beam and head seas.

2014), a method born in the field of precision engineering, that uses the concept of cumulative standard deviation (introduced in Section 4) to assess the effects of stochastic disturbances on a system's response. In this context, DEB provides in-depth knowledge that is crucial to explore means to improve workability.

In order to draw meaningful conclusions about the effect of environmental disturbances on the system response, all the possible weather combinations are taken into account. This results in the error budgeting clouds shown in Fig. 11, providing an indication of how the standard deviation of tower bottom motion builds-up over frequency. Please note that the opacity represents the probability of occurrence and the larger the gradient, the larger the contribution of the respective frequencies to wind turbine bottom motions.

The plots on the left column, in Fig. 11, refer to beam seas and the ones on the right to head seas. The first row shows error budgeting clouds for wind disturbances, since these ones do not depend on wave direction, both plots are analogous. The second row shows the contribution of wave induced motions to standard deviation. The bottom row refers to the motions caused by wind and waves simultaneously. The fading of the error budgeting clouds represents the probability of occurrence of each environmental condition. The dashed lines represent the weighted average of the clouds. From these results it is possible to immediately notice a difference in the scale of the vertical axis between beam and head waves. This is caused by significantly higher values of standard deviation in tower bottom motions in head seas, with sea-states causing standard deviations up to 20 meters. This is caused by the higher stiffness in pitch, with these results challenging the assumption of linearity behind the model. Nevertheless, it is an indication that for this system head waves are not a favourable condition, which is in line with the workability results shown earlier. When looking at wind induced motions, it is possible to observe that most of the contributions occur at around 0.3 rad/s, with maximum standard deviation reaching close to 3 m and a weighted average below 1 m. As mentioned, wave induced motions are highly dependent on wave direction. In beam waves, the wave contributions occur in two intervals: a narrow one close to 0.3 rad/s (same as wind induced motions); and a broad one ranging from 0.5 to 0.7 rad/s, containing the larger portion of the contributions. Furthermore, the standard deviation in beam waves is not expected to be over 6 m, and the weighted average converges about 1 m. In head waves it is different, with most of the contribution concentrated close to 0.4 rad/s, a maximum standard deviation of over 20 meters and a weighted average close to 3 m. When considering wind and waves simultaneously, it is possible to see that for the beam waves case most of the contributions end-up being concentrated at 0.3 rad/s while for head waves at 0.3 and mostly at 0.4 rad/s, with the weighted average converging to about 1 and 3 m, respectively. Overall the most contributing frequencies to tower motion are located in the range of 0.2 to 0.7 rad/s, with the main peaks at 0.3 and 0.4 rad/s. Wind acts on the lower range of this spectrum. Furthermore, these results back-up the workability analysis, where it is concluded that head-waves constitute a more challenging condition than beam waves, and workability is mainly limited by waves. Regarding the latter, it has been shown in literature that accounting for wave directional spreading can affect the performance of installation vessels (Buitendijk, 2016), given that it induces 3D motions on the ship and load. This should be addressed in future research.

Although these results show which frequencies contribute the most to tower motions, they do not explain which pendulation modes are being excited the most. For this purpose, Fig. 12 shows the Frequency Response Function (FRF) of the system: According to this FRF, is possible to conclude that the main pendulation mode is the first one. The natural frequency of the third pendulation mode occurs at around 4.5 rad/s, explaining its small relevance. It is also interesting to note the presence of anti-resonant dips from wind excitation to tower bottom motions, meaning that at these frequencies minimal tower bottom displacements are expected, in contrast to the resonance peaks.

6. Conclusions

In recent years attention has shifted to floating installation of OWT. This installation method overcomes some of the current limitations of jack-up vessels and allows conventional offshore heavy-lift contractors to enter the wind market. With the goal of creating a better understanding of this type of operations, this paper presents a validated open-source framework for floating installation of OWT towers and applies it to a case-study. A by-product of this work is the novel open-source crane-vessel, aimed at promoting open-research in this field (Domingos et al., 2023).

The framework is successfully validated using WEC-Sim. The results show a 2% over-estimation of the system response to the first pendulation mode, while the main contributing disturbance frequencies are predicted with no error. These results justify the use of a linear model with no tower to vessel interaction. The versatility of the framework is demonstrated by means of the case study in which the installation of a DTU 10 MW wind turbine tower on the Portuguese coast is analysed. Based on on-site records from 1990 to 2019, the results show that the

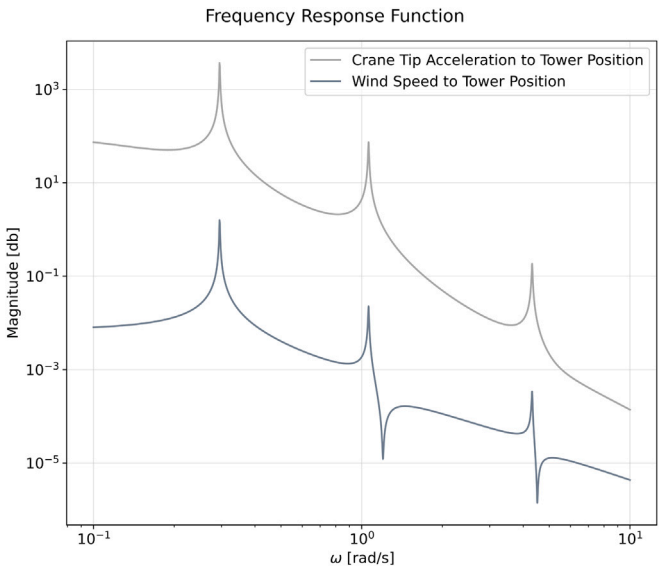

Fig. 12. Crane tip acceleration amplitude spectra and tower bottom position response to crane tip accelerations.

workability in beam-waves is higher than in head-waves, with an yearly value of 39%. The overall difference in workability between beam and head-waves comes from the higher hydrostatic stiffness in pitch, resulting in larger crane-tip accelerations. It is also shown that waves limit workability the most, except in the summer, and that positional installation tolerance is critical. Also, a projection based on these results and field data (Installation Time, 2023) indicates that it would take approximately 4 to 5 years for the wind farm in this case-study to be completed.

In order to better understand the influence of the system's parameters on tower motions, a sensitivity analysis based 1250 Monte Carlo simulations was performed. The results show that larger towers tend to reduce motions, which is explained by the reduction of the second pendulation mode. In contrast to this, tower motions tend to increase with block mass, since it reduces the natural frequency of the second pendulation mode, making it more vulnerable to environmental disturbances. Variations in this parameter do not affect motions as much as tower size, given that tower mass scales with L_t^3. Also the same analysis points in the direction that sling angle (ϕ_s) is a superfluous degree of freedom, which increases the computational cost of the model by over 50% while having very limited influence on tower motions. The third pendulation mode frequency is too high to be significantly excited in this case study.

While workability and sensitivity analyses provide a picture of the system's limitations and behaviour, an error budgeting analyses provides information about the most relevant frequencies exciting the system. Error budgeting clouds are computed for all the combinations of significant wave height, peak-period and mean wind speed, taking into account their probability of occurrence. Showing that, for this case-study, the main contributing frequencies for tower motions occur at 0.3 and 0.4 rad/s, with wind acting at the lower range of this spectrum.

This work contributes to existing literature by providing a better understanding of the susceptibility of floating installation of OWT towers to environmental conditions, in the context of an open-source case-study and framework.

CRediT authorship contribution statement

David Fidalgo Domingos: Writing – review & editing, Writing – original draft, Visualization, Validation, Software, Resources, Project administration, Methodology, Investigation, Formal analysis, Data curation, Conceptualization. **Peter Wellens:** Writing – review & editing, Validation, Supervision, Resources, Methodology, Formal analysis, Data curation, Conceptualization. **Jan-Willem van Wingerden:** Writing – review & editing, Validation, Supervision, Resources, Project administration, Methodology, Funding acquisition, Formal analysis, Data curation, Conceptualization.

Declaration of competing interest

The authors declare that they have no known competing financial interests or personal relationships that could have appeared to influence the work reported in this paper.

Data availability

Detailed data of the open-source reference crane-vessel Prometheus, can be found in the 4TU research repository, (Domingos et al., 2023).

Acknowledgements

This work is part of the "DOT 6000 - Floating Offshore installation XXL wind turbines", where Delft Offshore Turbine B.V., Heerema Marine Contractors Nederland SE and Techische Universiteit Delft have teamed up. Funding was provided by RVO, with the grant number TEHE119004. We further would like to acknowledge Rolf van Huffelen and Alejandro Velez Isaza, for supporting this research with their technical expertise in the field of offshore heavy-lift operations.

References

Active Heave Compensation, 2023. Seaqualize. [Online] Available: https://www.seaqualize.com/.

Ancellin, M., Dias, F., 2019. Capytaine: A python-based linear potential flow solver. J. Open Source Softw. 4 (36), 1341. http://dx.doi.org/10.21105/joss.01341.

Babarit, A., Delhommeau, G., 2015. "Theoretical and Numerical Aspects of the Open Source BEM Solver NEMOH". In: Proceedings of EWTEC. Nantes, France.

Bak, C., Zahle, F., Bitsche, R., Kim, T., Yde, A., Henriksen, L.C., Hansen, M.H., Blasques, J.P.A.A., Gaunaa, M., Natarajan, A., 2013. The DTU 10-MW Reference Wind Turbine. Technical Report, Technical University of Denmark.

Bianchi, F.D., Battista, H.D., Mantz, R.J., 2010. Wind Turbine Control Systems: Fundamental Concepts in Wind Turbine Engineering. Springer, http://dx.doi.org/10.1115/1.802601.ch14.

Bilgili, M., Alphan, H., 2022. Global growth in offshore wind turbine technology. Clean Technol. Environ. Policy 24 (7), 2215–2227.

Bishop, R., Hassan, A., 1964. The lift and drag forces on a circular cylinder oscillating in a flowing fluid. Proc. R. Soc. Lond. Ser. A Math. Phys. Eng. Sci. 277 (1368), 51–75. http://dx.doi.org/10.1098/rspa.1964.0005.

Bos, R., Wellens, P., 2021. Fluid-structure interaction between a pendulum and monochromatic waves. J. Fluids Struct. 100, 103191. http://dx.doi.org/10.1016/j.jfluidstructs.2020.103191.

Buitendijk, L., 2016. Floating Installation of Offshore Wind Turbine Foundations (Master's thesis). Delft University of Technology and Van Oord.

Clarenburg, J.B., 2014. Efficient Design of Controlled Offshore Systems (Master's thesis). Delft University of Technology.

Clauss, G., Riekert, T., 1990. Operational limitations of offshore crane vessels. In: Proceedings of Offshore Technology Conference. Houston, Texas, US, http://dx.doi.org/10.4043/6217-MS.

Cozijn, J., van der Wal, R., Dunlop, C., 2008. Model testing and complex numerical simulations for offshore installation. In: Proceedings of ISOPE. Vancouver, Canada.

de Kruif, B.J., Rossin, B., 2021. Pendulation control for dynamical positioning capable ship: Considerations on actuator usage. IFAC-PapersOnLine 54 (16), 120–125. http://dx.doi.org/10.1016/j.ifacol.2021.10.082.

der Male, P., Lourens, E.-M., 2015. Operational vibration-based response estimation for offshore wind lattice structures. In: Proceedings of the Society for Experimental Mechanics Series. pp. 83–96. http://dx.doi.org/10.1007/978-3-319-15230-1.

Domingos, D., Wellens, P., van Wingerden, J.W., 2023. Prometheus: An open-source sscv. http://dx.doi.org/10.4121/aa0a24fc-b7e2-4e05-b0cb-f1dc2af1c9ac, 4TU.ResearchData.

ESOX, 2023. Lautec. [Online]Available: https://esox.lautec.com/map/.

Gao, Z., Verma, A., Zhao, Y., Jiang, Z., Ren, Z., 2018. A summary of the recent work at NTNU on marine operations related to installation of offshore wind turbines. In: Proceedings OMAE. Madrid, Spain.

Hong, S., Zhang, H., Halse, K.H., 2023. Hydrodynamic and environmental modelling influence on numerical analysis of an innovative installation method for floating wind. Ocean Eng. 280, 114681. http://dx.doi.org/10.1016/j.oceaneng.2023.114681.

Hoogendoorn, G., Van Den Bos, W., Polinder, H., 2021. Design in principle of crane vessel for flexible fully assembled wind turbine installation. In: Proceedings of International Conference on Advanced Intelligent Mechatronics. IEEE, pp. 1083–1088.

Installation Time, 2023. Spinergie. [Online] Available: https://www.spinergie.com/resources/offshore-wind-installation-time.

Jabben, L., van Eijk, J., 2011. Performance analysis and design of mechatrnic systems. Mikroniek 51, 5–12.

Jiang, Z., Gao, Z., Ren, Z., Li, Y., Duan, L., 2018. A parametric study on the final blade installation process for monopile wind turbines under rough environmental conditions. Eng. Struct. 172, 1042–1056.

Johan Åström, K., Murray, R.M., 2021. Feedback Systems: An Introduction for Scientists and Engineers. Princeton University Press, http://dx.doi.org/10.5860/choice.46-2107.

Journée, J.M.J., Massie, W.W., Huijsmans, R.H.M., 2015. Offshore Hydromechanics. Delft University of Technology.

Kroft, B., Wellens, P., Bokhorst, J., van Dijk, R., 2022. Motion Prediction of a Semi-Submersible Crane Vessel at Inconvenient Draft (Master's thesis). Delft University of Technology.

Ku, N.K., Cha, J.H., Roh, M.I., Lee, K.Y., 2013. A tagline proportional-derivative control method for the anti-swing motion of a heavy load suspended by a floating crane in waves. Eng. Marit. Environ. 227 (4), 357–366.

Kundo, P., Cohen, I., Dowling, D., 2016. Fluid Mechanics. Elsevier, http://dx.doi.org/10.1016/C2012-0-00611-4.

Lu, J.Y., Mony, S.K., Carlsen, H., Sixtensson, C., 2011. Solution to design challenges and selections of wind turbine installation vessels. In: Proceedings of Offshore Technology Conference. Houston, Texas, USA.

Makarov, O., Harada, T., 2022. Effective approach to modeling the hydrodynamic response of a multibody system with suspended load in the time domain. In: Proceedings of Jc-IFToMM. Kyoto, Japan, pp. 95–102. http://dx.doi.org/10.57272/jciftomm.5.0_95.

Map Viewer, 2023. European marine observation and data network. [Online] Available: https://emodnet.ec.europa.eu/geoviewer/.

Marelli, S., Lamas, C., Konakli, K., Mylonas, C., Wiederkehr, P., Sudret, B., 2022a. UQLab: A Framework for Uncertainty Quantification in Matlab. Technical Report, ETH Zurich, http://dx.doi.org/10.1061/9780784413609.257.

Marelli, S., Lamas, C., Konakli, K., Mylonas, C., Wiederkehr, P., Sudret, B., 2022b. UQLab user manual - Sensitivity analysis. Technical Report, ETH Zurich.

Meloni, C., Dellino, G., 2015. Uncertainty Management in Simulation-Optimization of Complex Systems: Algorithms and Applications. Elsevier, http://dx.doi.org/10.1007/978-1-4899-7547-8.

Meskers, G., van Dijk, R., 2012. A damping tugger system for offshore heavy lifts. In: Proceedings of OMAE, Vol. 44885. American Society of Mechanical Engineers, pp. 315–323.

Ministerios: Economia e Mar, Ambiente e Acao Climatica e, Infraestruturas e Habitacao, 2023. Proposta Preliminar das Areas Espacializadas e dos Pontos para a Ligação à Rede Nacional de Transporte de Eletricidade. Technical Report, Republica Portuguesa.

Nejad, A.R., Li, L., Acero, W.I.G., Moan, T., 2018. A systematic design approach of gripper's hydraulic system utilized in offshore wind turbine monopile installation. In: Proceedings of OMAE, Vol. 11A. pp. 1–10. http://dx.doi.org/10.1115/OMAE2018-77228.

Neupert, J., Mahl, T., Haessig, B., Sawodny, O., Schneider, K., 2008. A heave compensation approach for offshore cranes. In: Proceedings of ACC, Vol. 44885. IEEE, pp. 538–543.

Next Generation Jack-Up, V., 2023. Jan de nul. [Online] Available:https://www.jandenul.com/news/jan-de-nul-launched-worlds-tallest-next-generation-jack-installation-vessel-voltaire/.

Nojiri, N., Sasaki, T., 1983. Motion characteristics of crane vessels in lifting operation. In: Proceedings of Offshore Technology Conference. OnePetro.

Offshore Renewable Energy, 2023. European union. [Online] Available: https://energy.ec.europa.eu/topics/renewable-energy/offshore-renewable-energy_en.

Ogden, D., Ruehl, K., Yu, Y.H., Keester, A., Forbush, D., Leon, J., Tom, N., 2022. Review of WEC-sim development and applications. Int. Mar. Energy J. 5 (3), http://dx.doi.org/10.36688/imej.5.293-303.

Portugal to Launch First Offshore Wind Auction, Eyes 10 GW by 2030, 2023. Reuters. [Online] Available: Portugal to launch first offshore wind auction, eyes 10 GW by 2030.

Pratt, J.A., Priest, T., Castaneda, C.J., 1997. Offshore Pioneers: Brown & Root and the History of Offshore Oil and Gas. Elsevier.

Ramirez, L., Fraile, D., Brindley, G., 2019. Offshore Wind in Europe. Technical Report, WindEurope.

Ren, Z., Jiang, Z., Gao, Z., Skjetne, R., 2018a. Active tugger line force control for single blade installation. Wind Energy J. 21 (12), 1344–1358. http://dx.doi.org/10.1002/we.2258.

Ren, Z., Skjetne, R., Gao, Z., 2018b. A crane overload protection controller for blade lifting operation based on model predictive control. Energies 12 (1), 50.

Ren, Z., Skjetne, R., Jiang, Z., Gao, Z., Shankar, A., 2019. Integrated GNSS/IMU hub motion estimator for offshore wind turbine blade installation. Mech. Syst. Signal Process. 123, 222–243. http://dx.doi.org/10.1016/j.ymssp.2019.01.008.

Salome Mesh User's guide: Introduction to Mesh, 2023. Salome. [Online] Available: https://docs.salome-platform.org/latest/main/index.html.

Schepers, J., Domingos, D., ter Braak, J., van Winsen, I., van Wingerden, J.W., 2022. Design of gain-scheduling cascade control for a motion compensated gripper frame. J. Phys. Conf. Ser. 2265 (3), 032082. http://dx.doi.org/10.1088/1742-6596/2265/3/032082.

TU Delft on Board the World Largest Crane Vessel for Exploring Future Offshore Wind Turbines, 2023. Delft university of technology. [Online] Available: https://www.tudelft.nl/en/2021/3me/october/tu-delft-on-board-the-world-largest-crane-vessel-for-exploring-future-offshore-wind-turbines.

van Beek, M., van Dijk, R., van Dalen, K., Metrikine, A., 2018. A Feasibility Study for the Installation of 10 MW Offshore Wind Turbines with an SSCV (Master's thesis). Delft University of Technology.